MR-conditional Robotic Cardiac Intervention: Design and Validation in Patient-specific Phantoms

Yaxi Wang[1], *Student member, IEEE*, Enhui Yong[2], Wenlong Gaozhang[1], Vivek Muthurangu[2] and Helge A Wurdemann[1], *Member, IEEE*

***Abstract*—Manual hand-held catheterization by clinicians under Magnetic Resonance Imaging (MRI) has become popular for the treatment of cardiovascular diseases such as pulmonary edema and heart failure. However, the limited space of the MRI bore makes it challenging for clinicians to access the opening, and the prolonged operation can cause back injury. To implement MRI-guided robot-assisted catheterization, this paper presents an MR-conditional robotic system for right heart catheterization (MR-RHC). Our 2-degree-of-freedom (DoF) robotic manipulator is actuated by ultrasonic piezoelectric motors. The highly compact design ($D\times\ W\times\ L=11\,\text{cm}\times\ 8\,\text{cm}\times\ 18\,\text{cm}$) allows the robot to be positioned in the MRI scanner bore, near the patient's femoral vein opening. The contribution of this paper lies in the development of an MR-conditional robotic system that clinically required Swan-Ganz catheter movements, including (simultaneous) infinite continuous rotation and translation (i.e., the catheter can perform endless rotation and translation that are not restricted by cable tangling or limited operational motion of the actuators). The MR conditionality of the robotic system is demonstrated in a clinical MR environment. Additionally, the system has been characterized in terms of its force and torque capabilities and verified 100% success rate of tele-intervention within 7 patient specific phantoms. Lastly, the paper reports the intervention of an MRI-guided robot-operated catheter within the water-filled phantoms between the control room and MR scanner.**

***Index Terms*—MR-conditional robotics, cardiovascular disease, flexible catheter, interventional robotics.**

I. Introduction

CARDIOVASCULAR diseases (CVDs) are a leading cause of human mortality. In 2021, CVDs were responsible for 20.5 million deaths, accounting for approximately a third of global fatalities and maintaining their position as the primary cause of human mortality [1], [2]. One technique for both diagnosis and interventions in CVDs is cardiac catheterization. Here, a catheter is inserted into the heart or vasculature, which can be used to measure pressure, perform angiography, or carry out interventions such as balloon angioplasty/stenting. Cardiovascular catheterization is conventionally guided using X-ray fluoroscopy, providing clinicians with visualization of both catheters and, to a limited extent, cardiovascular soft tissues [3]. However, there are disadvantages of X-ray fluoroscopy, including exposure to ionizing radiation and poor soft tissue contrast. Magnetic Resonance Imaging (MRI) has emerged as a promising modality for guiding cardiac catheterization [4], offering distinct advantages beyond its non-radiative nature. MRI provides high resolution of soft tissue, enabling detailed visualization of cardiac/vascular structures, without the need for contrast agents [5]. These capabilities make MRI well-suited for cardiac intervention procedures, enhancing anatomical assessment and procedural precision.

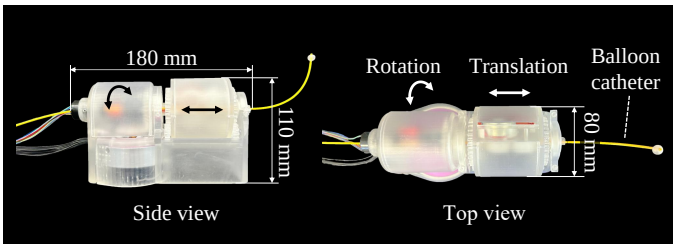

(a) Prototype of the MR-conditional robot including console

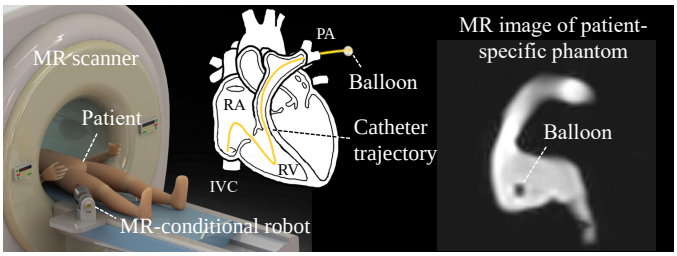

(b) Interventional application: RHC under MR guidance

Fig. 1. Prototype of the MR-conditional robot and illustration of its application for right heart catheterization (MR-RHC). (a) Side and top view of the robot showing the dimensions of our MR-conditional robot that are $D\times\ W\times\ L=11\,\text{cm}\times\ 8\,\text{cm}\times\ 18\,\text{cm}$. Using two piezoelectric motors, the teleoperated 2-DoF robot is capable to advance or pull back as well as rotate a commercially available balloon catheter. (b) Illustration of the interventional application of robotic right heart catheterization inside an MR scanner, in which the catheter balloon is navigated from the inferior vena cava (IVC), through the right atrium (RA), and right ventricle (RV), and finally arrives in the pulmonary artery (PA).

A. State-of-Art of MR-conditional catheter/needle robotics

MR-conditional robotic intervention systems have been successfully employed in various interventional procedures. Table I summarizes related MRI-guided robotic-assisted catheter/needle intervention systems. Notable examples include neurosurgery, prostate, breast biopsy, endovascular/cardiovascular and orthopedic intervention [6], [7]. For

This work is supported by the Springboard Award of the Academy of Medical Sciences (grant number: SBF003-1109), the Engineering and Physical Sciences Research Council (grant numbers: EP/R037795/1, EP/S014039/1 and EP/V01062X/1), the Royal Free Hospital, London, UK, The UCL Dean's Prize, UCL Mechanical Engineering.

[1]Yaxi Wang, Wenlong Gaozhang and Helge A. Wurdemann are with the Department of Mechanical Engineering, University College London, UK. (emails: yaxi.wang.21@ucl.ac.uk; h.wurdemann@ucl.ac.uk).

[2]Enhui Yong and Vivek Muthurangu are with the Institute of Cardiovascular Science, University College London, London, UK.

TABLE I
SUMMARY OF MR-CONDITIONAL INTERVENTIONAL ROBOTS

Ref. and Key authors	Procedures	DoF	Robot	Actuation	Validation	Inf cont translation	Inf cont rotation	Concurrent
[8] G. Li.et al. (2015)	Neurosurgery	3	Needle	Piezoelectric	In-vitro phantom	✔	N/A	N/A
[14] Y. Kim.et al. (2017)	Neurosurgery	2	Catheter	SMA actuator	Gelatin test	✔	N/A	N/A
[9] N. Patel.et al. (2020)	Neurosurgery	3	Needle	Piezoelectric	In-porcine trial	✔	N/A	N/A
[10] Z. He et al. (2024)	Neurosurgery	3	Needle	Pneumatic	In-cadaver	✔	N/A	N/A
[11] H. Su et al. (2015)	Prostate	6	Needle	Piezoelectric	In-vitro phantom	✔	✗	✔
[12] H. Liang et al. (2024)	Prostate	3	Needle	Pneumatic	In-vitro phantom	✔	N/A	✔
[13] B. Yang et al. (2014)	Breast biopsy	5	Needle	Pneumatic	In-vivo	✔	N/A	N/A
[15] V. Groenhuis et al. (2017)	Breast biopsy	3	Needle	Pneumatic	In-vitro phantom	✔	N/A	N/A
[16] G. Li et al. (2020)	Orthopaedic	6	Needle	Pneumatic	In-vitro phantom	✔	✗	✔
[17] T. Liu et al. (2017)	Cardiovascular	3	Catheter	Magnetic	In-vitro phantom	N/A	N/A	N/A
[18] Lee et al. (2018)	Cardiovascular	2	Catheter	Hydraulic	In-vitro phantom	✔	✗	✔
[19] Tavallaei et al. (2016)	Endovascular	2	Catheter	Piezoelectric	In-vitro phantom	✔	✔	✔
[20] D. Kundrat et al. (2021)	Endovascular	2	Catheter	Pneumatic	In-vitro phantom	✗	✔	✗
[21] G. Dagnino et al. (2023)	Endovascular	2	Catheter	Pneumatic	In-vivo animal	✗	✔	✗
[22] Z. Dong et al. (2022)	Cardiovascular	2	Catheter	Hydraulic	In-vitro phantom	✔	✗	✔
This Work	Cardiovascular	2	Catheter	Piezoelectric	Patient phantom	✔	✔	✔

instance, G. Li et al. developed a 3-DoF MR-conditional neurosurgical intervention robot, which uses piezoelectric actuators to achieve improved accuracy and enhanced safety compared to manual manipulation under MRI guidance [8]. They demonstrated a 15% signal-to-noise ratio (SNR) variation and confirmed the absence of image artifacts in a clinical MRI device. Building on this, N. Patel et al. conducted a preclinical evaluation of robotic interventions for neurosurgery, reporting translational and rotational errors of 3.13 mm and 5.58 mm, respectively, in repetitive procedures using a porcine model [9]. Furthermore, Z. He et al. developed a soft actuator designed for neurosurgery, integrated with a multi-stage stereoscopic robotic positioner [10]. This ensured sufficient working space for soft robotic interventions and was validated in cadaveric studies with an aiming accuracy of less than 3.0 mm. MRI-guided prostate puncture interventions have also gained popularity as clinical techniques. For example, H. Su et al. developed a 6-DoF robot for prostate interventions using piezoelectric motors [11]. Phantom-based interventional experiments showed a 3D operation error of only 0.87 mm, with an SNR loss within 15%. Similarly, H. Liang et al. designed an MR-safe pneumatic robot for prostate biopsies, achieving a target position accuracy of 1.3 mm and an SNR variation of less than 5% in a 3T MRI environment [12]. In addition, B. Yang et al. designed an MR-conditional leader-follower robotic system for MRI-guided breast biopsy, which uses a parallel mechanism with pneumatic actuation for needle insertion and steering. Targeted experiments were implemented in vivo in anesthetized pigs without artifacts [13].

For MRI-guided interventional endovascular/cardiovascular robotics, Lee et al. proposed an MR-safe, hydraulically driven intracardiac catheterization robot for remote operation of electrophysiological (EP) interventions. This system has 2-DOF (translation and rotation) [18], [23] and enabled real-time catheter tip tracking in the MRI environment with no issues regarding MRI conditionality [22]. However, its structure makes it challenging to be used in MRI bore for MR-RHC. Kundrat et al. designed an MR-conditional pneumatic endovascular robotic manipulation platform that mimics the clinicians' movements for translation and rotation of EP catheters and provides intravascular haptic feedback, which is highly efficient and has a success rate of 90% [20], [24]. This is a ground-breaking design for the development of an EP intervention robot using space-consuming pneumatics as the actuation [25]. Although hydraulic and pneumatic actuation are prevalent methods for developing robots that are MR-conditional, piezoelectric ultrasound motors (USMs) are also suitable. USMs are compact and highly accurate, making them well suited to catheter manipulation in MRI environments. USMs have been increasingly used in cardio interventions, breast interventions and MR-safe robotic systems for neurosurgery [9], [26]–[29]. Tavallaei et al. proposed a 3-DOF MR-conditional catheter navigation system for cardiac catheterization based on USMs [19], [30]. The design of the leader-follower structure allows for accurate catheter navigation and the addition of plunger manipulation for catheterization.

B. Clinical requirement

MRI-guided Right Heart Catheterization (RHC), also known as Pulmonary Artery Catheterization (PAC), involves navigating the catheter through the inferior vena cava (IVC), right atrium (RA), and right ventricle (RV), reaching the pulmonary artery (PA). Distinct from other catheter types, PA catheters inherently possess a curved section, eliminating the need for an active steering device for orientation adjustments. Nonetheless, conducting MR-RHC presents notable challenges, among which restricted access to the patient within the scanner bore stands out. This limitation complicates clinicians' ability to reach vascular access sheaths at critical points such as the groin or neck, a difficulty further exacerbated in pediatric

patients, including children and infants. A promising solution to this accessibility issue in MR-RHC is the adoption of a robotic catheterization system positioned proximately to the patient. Existing robotic systems like Magellan and Sensei X (Hansen Medical, USA), designed for X-ray guided cardiac catheterization, already demonstrate the feasibility of minimizing clinician radiation exposure. Developing a similar system tailored for MR-RHC appears viable. Such a system would need to replicate clinician maneuvers, including catheter advancement, pullback, and rotation [31].

Table I [18]–[22] gives an overview of MR-conditional robotic platforms developed for endovascular/cardiovascular interventions. The table compares key specifications of systems including the actuation type, DoFs, and infinite continuous rotational/translational and concurrent motion (Inf con translation/rotation). The dimensions of existing follower robotic systems ([18]: 780 mm × 105 mm × 210 mm, [20]: 520 mm × 140 mm × 120 mm) require their positioning outside the MRI scanner due to space limitations. Furthermore, few current platforms are capable to provide (simultaneous) infinite continuous rotation/translation. However, for RHC procedures, a robotic MR-conditional robotic platform should offer aforementioned motion capabilities (evident from empirical data in Section II-A), and should be compact to be placed within the MRI scanner bore, allowing PA access through any vein (e.g., femoral, jugular, antecubital, or brachial).

C. Contribution

This paper introduces a 2-DOF MR-conditional catheterization robotic system that enables (simultaneous) infinite continuous movement (i.e., rotation and translation) of an inserted catheter (i.e., the catheter can perform endless rotation and translation that are not restricted by cable tangling or limited operational motion of the actuators). Two USMs supply rotational and translations motion to the catheter. An MR-conditional slip ring ensures that wires of the rotational part will spin with the slip ring. A compact design of the robotic manipulator ensures the flexibility of positioning the device outside or inside the MR scanner bore. We have experimentally verified the MR conditionality of the robot when working inside the MR scanner. In addition, robotic teleoperation in the MRI settings for intra-phantom interventions has been implemented and analyzed. Our contribution are:

- An MR-conditional robotic manipulator for flexible, pre-curved catheter was designed and fabricated, enabling (simultaneous) infinite continuous translational and rotational movement of inserted Swan-Ganz catheter. The robot is validated in clinical MRI settings as being MR-conditional ($< 3.5\%$ SNR variation) (see Section II and Section III-B).
- MRI-guided robotic teleoperation was successfully implemented for patient-specific phantom's interventions (see Section III-C). Robotic teleoperation of RHCs demonstrate enhanced robustness and consistency over clinical expert's manual operation (see Section III-D).

Section II sets out with an analysis of manual RHC resulting in a list of design requirements, together with material constraints and based on MRI scanner bore measurements, including a detailed design description of our MR-conditional interventional robot. The results of a number of experiments, partially for the MRI-guided robotic tele-intervention in patient-specific water-filled phantoms, are reported on in Section III. Section IV discusses the experiments and Section V is the conclusion and future work.

II. Design of the MR-conditional catheterization robotic system

A. Analysis of manual RHC by clinical expert

To understand the catheter translational and rotational movements during a manual RHC procedure, a number of experiments were conducted, involving an expert with over 20 years of experience in cardiovascular interventions. This study was approved by the Humanities, Arts and Sciences Research Ethics Committee under Project ID 0387.

The clinical expert was asked to navigate a Swan-Ganz catheter, that has an embedded balloon at its pre-bent tip, within 7 patient-specific phantoms, targeting the PA as illustrated in Fig. 2(a) and repeating the procedure 10 times for each phantom. To monitor the input (i.e. translational and rotational motion) from the clinician to the catheter, an NDI Aurora tracking system (Aurora, NDI, Canada) was placed beneath the setup and a 6-DoF tracker was mounted along the catheter. It is worth mentioning that we also explored force and torque values exerted throughout RHC. The experimental setup is shown in Fig. 2(b). We incorporated an IIT-FT17 6-DoF Force/Torque (F/T, Force accuracy: $\pm 0.1\%$ of ± 50 N, Torque accuracy: $\pm 0.1\%$ of ± 0.5 N · m) sensor to record force and torque. During manual operation, the catheter is first inserted into a clinical catheter sheath, which is mounted on the F/T sensor and connected to the phantom environment via a soft silicone tube. This setup ensures that the forces and torques applied to the catheter are transmitted through the sheath to the F/T sensor. A total of 10 RHC procedures were manually performed for each patient-specific phantom. The results of

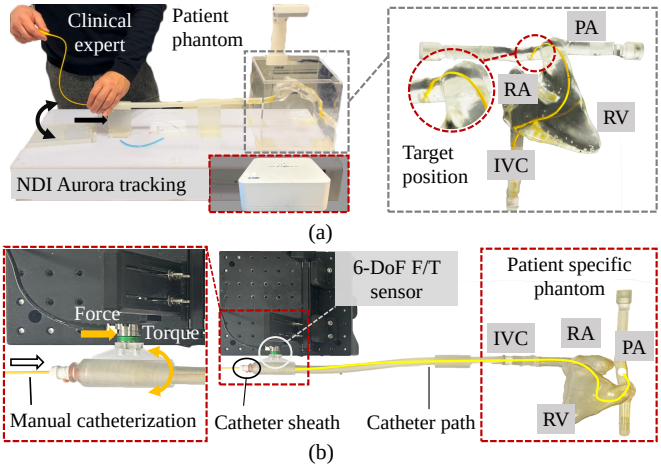

Fig. 2. Experimental setup (a) to analyze manual RHC performed by clinical expert, (b) measures the driving force and rotation torque on the catheter during expert manual RHC procedure in patient-specific phantoms.

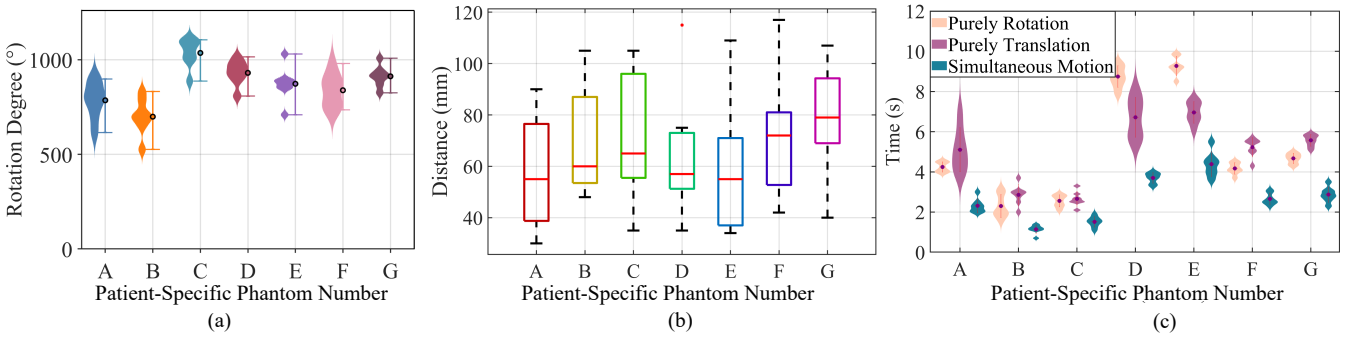

Fig. 3. Results for manual RHC inside 7 phantoms (A-G), repeated 10 times: (a) Accumulated angular range of catheter. (b) Distribution of translational motion for each step when continuously advancing. (c) Total time for decoupled (purely rotation/translation) and simultaneous translation and rotation.

the manual RHC analysis conducted by the clinical expert in this section will be compared with the robotic operation in Experiment 4 (Section III-D: Comparison of Manual and Robotic Operation)

Fig. 3 reports on the results of the translational and rotational inputs by the expert during manual intervention. Results are presented for each of the 7 phantoms (i.e. A-G). Fig. 3(a) specifies the angular range of the catheter, showing that for RHC procedures, the required unidirectional rotation angle falls within the range of 525° - 1105°. This underscores the necessity for the catheter to achieve a multiple turns of rotation. Fig. 3(b) illustrates the distribution of translational distances for each step of the expert manual operation, with results indicating variations between $37-96\,\mathrm{mm}$. Fig. 3(c) accumulates the time that the clinician either rotates or translates the catheter or inputs simultaneous rotation and translation during a single procedure. The results indicate that the clinical exert inputs decoupled and simultaneous rotational and translational movement to the Swan-Ganz catheter.

B. Requirements for MR-RHC and the robot design

The design of the catheterization robot involves taking into account material constraints, dimensional specifications of MRI scanners as well as the results presented in Section II-A. These overall requirements can be summarized as follows:

1) MR conditionality: In order to ensure the avoidance of image artifacts and interference during MR-RHC, the robotic system should be made of non-ferromagnetic components to prevent substantial RF artifacts.
2) Compact design: The approximate dimensions of an MRI scanner (e.g., a 1.5T, Siemens MAGNETOM Aera, Siemens Healthineers, Germany) bore are $\varnothing \times \ L = 70\,\mathrm{cm} \times \ 137\,\mathrm{cm}$. The available space for the placement and operation of the robotic manipulator is significantly limited once the patient is positioned inside the MRI scanner bore. To address space challenges enabling the robot to be operated within the MRI bore, a compact design of the robot is required as it enables seamless entry into the MRI bore and allows for close operation near the patient's vascular access sheath.
3) (Simultaneous) infinite continuous movements: Navigating a catheter along a complex path to the pulmonary artery requires decoupled and simultaneous rotational and translational movement, i.e., multi-turn rotation and a continuous translation of up to 96 mm (see Section II-A).

C. Design of the MR-conditional robotic manipulator

Considering dimensional requirements for RHC and latency challenges of hydraulic and pneumatic actuation systems when connecting long tubes between the MRI and control room, we employed ultrasonic piezoelectric motors (USMs) for robotic actuation. USMs ensure instantaneous and precise actuation and are MR-conditional. Prominent examples include MR-guided interventions in prostate, neurosurgery and brain procedures [11], [13], [32]–[34].

To enable advancement and pullback motion, the WLG-30 non-magnetic motor (Tekceleo, France. Holding torque, $125\,\mathrm{mN\cdot m}$) was integrated. For catheter rotational movement, the WLG-75 (Tekceleo, France. Holding torque, $1500\,\mathrm{mN\cdot m}$) non-magnetic motor was incorporated. These motors have been integrated into a compact structure with an overall dimension of $D \times \ W \times \ L = 11.5\,\mathrm{cm} \times \ 9\,\mathrm{cm} \times \ 13\,\mathrm{cm}$. An integrated CAD model of an MR-conditional 2-DoF robot is presented in Fig. 4(a). The robot includes a 3D printed main support structure (Draft Resin, Formlabs, USA), two ultrasonic piezoelectric motors, MR-safe plastic bearings, 3D printed gears, active-passive rollers and an 8-circuits slip ring.

Fig. 4(b) shows a close-up view of the rotational part. In PAC procedures, there is a need for robotic systems capable of replicating the rotational movements performed by clinicians while manipulating the handheld catheter. Though there is no active steering mechanism, a CE-marked, commercially available PA catheter comprises a curved section with a balloon at its tip. Rotating this curved section influences the direction of the advancement of the catheter tip during a procedure. In order to facilitate simultaneous advancement and rotation of the catheter, the rotational part is integrated with the translational component. The rotational part of the robot is executed by the WLG-75 motor transfers the rotational motion to the translating part utilizing two gears. To address the challenge of wire entanglement when unlimited rotation is being achieved between the motor wires and the catheter, an 8-circuits MR-conditional slip ring (JINPAT Electronics CO.LTD, China) has been incorporated into the design. The

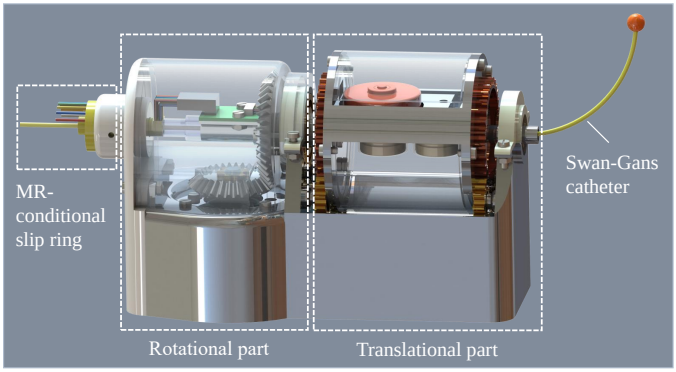

(a) 2-DoF MR-conditional interventional robot

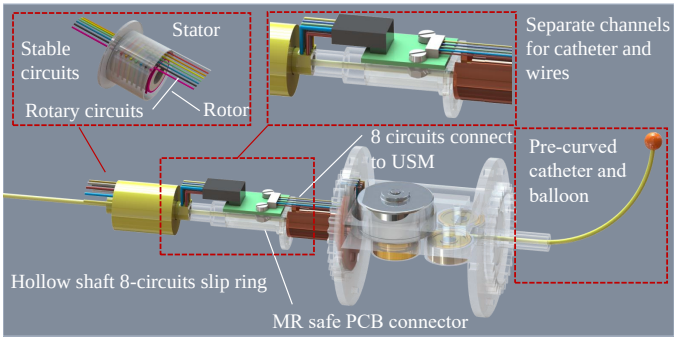

(b) 8-circuits MR-conditional slip ring connect to USM

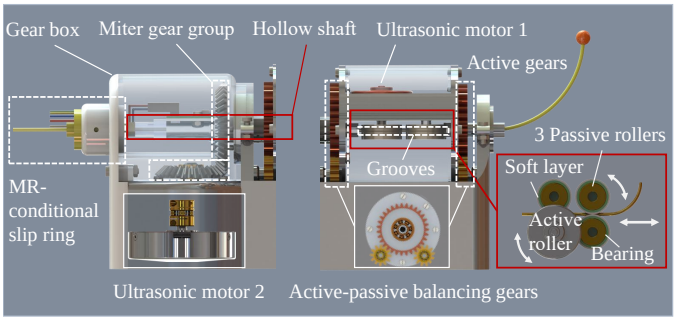

(c) Rotational part (d) Translational part

Fig. 4. CAD model of 2-DOF MR-conditional interventional robot. (a) Overall 2-degree-of-freedom MR-conditional interventional robots, including the (b) MR-conditional 8-circuits slip ring connecting the translational part for catheter unlimited rotation. (c) rotational part (made of ultrasonic motor, miter gear group, active-passive balancing gears) and translational part (made of an ultrasonic motor, active-passive rollers and MR-Safe bearings etc.).

slip ring is composed of plastic and aluminum alloy materials. During integration into the robot and connection to the motor wire, the motor wires and the catheter are positioned within the central and outer channels, respectively. This configuration will eliminate the issue of the interference between motor wire and catheter during concurrent operation, providing infinite catheter rotation.

Fig. 4(c) and (d) show the CAD models of the translational and rotational robotic parts, delivering simultaneous translation (advancement/pullback motion) and rotation. The robot joystick console were designed to connect the robot manipulator via MR-conditional extension cables (length, 10 m), allowing clinicians to navigate the MR-conditional robotic manipulator remotely from the main control room. For the translational part in Fig. 4(d), the WLG-30 non-magnetic motor was integrated (maximum rotational speed of 250 rev/min). To facilitate the transfer of rotational motion to catheter advancement, an active-passive roller system has been created comprised of four rollers (1 active roller and 3 passive rollers) that clamp the catheter in place. The incorporation of a 1 mm diameter groove between the four rollers ensures a predetermined path for the catheter, effectively preventing any misalignment during operation. Furthermore, a soft layer covers the roller surfaces, enhancing drive friction and preventing the catheter against any compression caused by the rigid rollers. The active-passive roller set of the translational part remains continuously clamped to the catheter and is actuated by Ultrasonic Motor 1, which is connected to the MR-conditional slip ring. The translational part is mechanically coupled to to the rotational part by the Ultrasonic Motor 2 (See Fig.4(c)). As a result, when the rotational part manipulates the catheter, the translational part follows its motion. Concurrent translation and rotation of the catheter can be performed when both parts are working simultaneously.

III. Experimental Setups and Results

This section presents the validation of the robotic operation for patient-specific phantoms. Experiment 1 evaluates the force and torque performance of the robot manipulator. Experiment 2 assesses the MR conditionality. Experiment 3 validates the MRI-guided robotic teleoperation. Experiment 4 compares the manual operation with robotic operation.

A. Experiment 1- Force and torque evaluation

1) Experimental protocol: Fig. 5(a) presents the experimental setup used to measure the driving force generated by

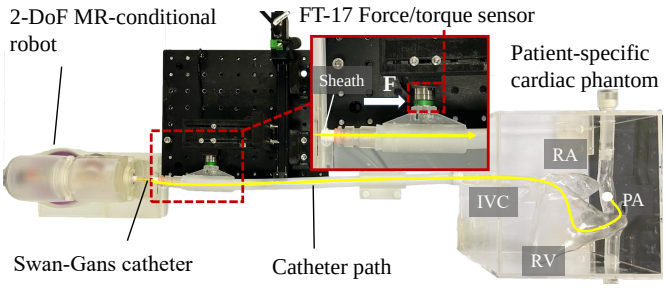

(a)

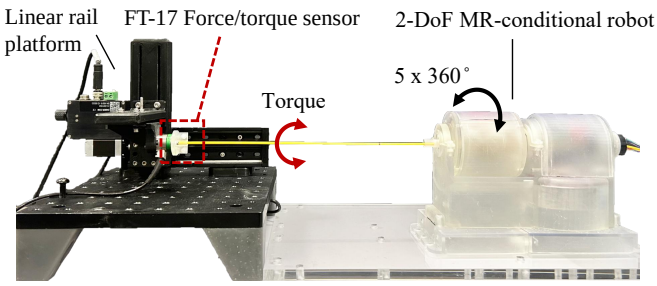

(b)

Fig. 5. Experiment 1 setup: (a) The F/T sensor measures the driving force applied by the robot during catheter manipulation. (b)The F/T sensor measures the torque exerted by the robot for catheter rotation.

the robot. The 6-DoF Force/Torque (F/T) sensor was aligned with the robot and connected to the catheter sheath, which was suspended and loosely coupled to the phantom via a soft silicone tube. During robotic operation, the catheter was inserted into the clinical sheath, and the robot - controlled via a joystick console - advanced the catheter through the sheath toward the pulmonary artery (PA) of the phantom. This setup ensured that the driving force exerted by the robot was transmitted through the sheath and captured by the F/T sensor. The value of the radial force was then recorded by the F/T sensor. To increase the actuation capability of the robot, this study used Ecoflex-0050 (Silicone rubber, Smooth-On, USA) soft material layers moulding with 3 thicknesses of 1.0 mm, 1.5 mm, and 2.0 mm on the active-passive rollers. The test was repeated 20 times for each thickness. The value of the driving force of the catheter was recorded during $0-600$ mm travel with a constant motor speed of 20 rev/min.

Fig. 5(b) shows the setup for testing the holding torque generated by the robot. The catheter tip was connected to the F/T sensor platform. The robot manipulates the catheter to rotate $5 \cdot 360$ degrees, recording the torque generated by the robot on the catheter. To investigate the effect of the thickness of the soft material layers embedded in the active-passive rollers on the holding torque, similarly to the evaluation test of the driving force, the torque was then measured by varying the thickness of the soft layers affixed to the robot's active - passive rollers. The speed of the WLG-75 ultrasonic motor is set at 20 rev/min. The holding torque is measured for each thickness for 20 repetitions and then recorded by F/T sensor.

2) Results for Experiment 1: Fig. 6(a) presents the measurement of the driving force on the catheter caused by robotic teleoperation and manual operation by the expert, as conducted in Section II-A. The blue dotted line signifies the manual driving force within the catheter's $0-600$ mm travel range, picking the maximum value of the driving force for each phase at 100 mm interval. The orange solid line represents the robot's driving force on the catheter with a soft layer thickness of 1.0 mm. Similarly, the yellow and purple solid lines denote the driving forces at soft layer thicknesses of 1.5 mm and 2.0 mm, respectively. The experimental results indicate that the driving force on the catheter increases with the travel distance before plateauing, with the maximum driving force needed for manual intervention completion being 3.9 N. In robotic operation, the driving force exerted by the robot on the catheter increases with the thickness of the soft silicone layer at a given rotational speed. This force trend closely mirrors manual operations, achieving maximum forces of 4.2 N, 4.77 N, and 5.35 N at thicknesses of 1.0 mm, 1.5 mm, and 2.0 mm, respectively.

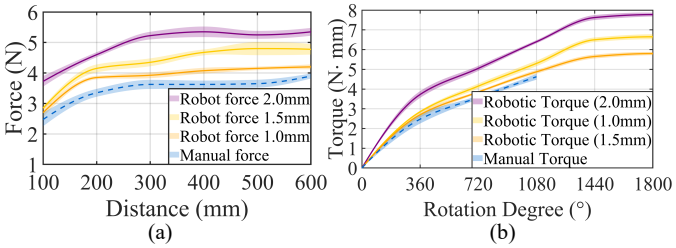

Fig. 6. Experiment 1 results: (a) Evaluation of driving force generated by rollers with an outer surface of soft material of a 1 mm, 1.5 mm and 2 mm thickness. (b) Robot-operated catheter output torque.

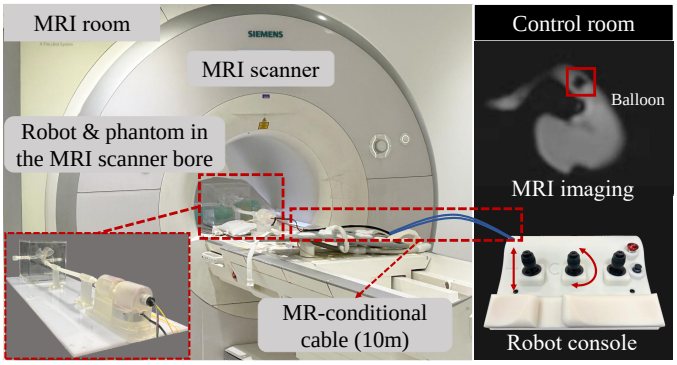

(a) Experiment 2 and 3 setup: MR conditionality & MRI teleoperation

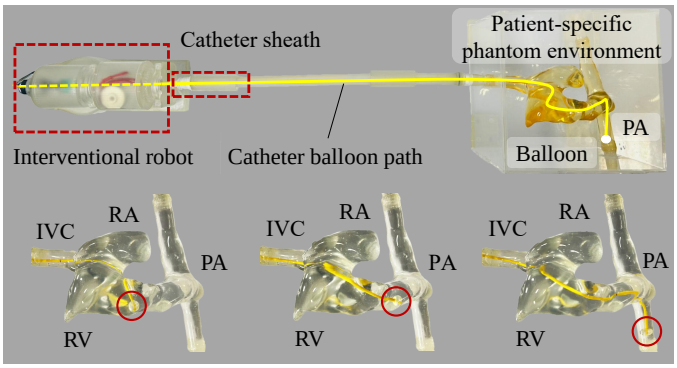

(b) Top view of the robot & phantom and catheter navigation

Fig. 7. Experiment 2 and 3 setup: MR conditionality test and robotic teleoperation. (a) The water-filled phantoms and robot was placed in the MRI scanner bore. MR-safe extension cables were connected to the console in the control room. The clinician operates joysticks (bottom right) to perform catheter intervention, guided by real-time balloon visual feedback displayed on the monitor (top right). (b) Top view of the robot with patient-specific phantom and catheter navigation.

Fig. 6(b) shows the variation of the torque on the catheter during robotic teleoperation and manual manipulation by the expert (as described in Section II-A). The dotted blue line shows that in expert manual operations, the catheter's torque increases with the rotation angle, reaching a maximum of $4.63\,\mathrm{N}\cdot\mathrm{mm}$ over repeated procedures. For the same degree of rotation the torque from robotic operation was $4.875\,\mathrm{N}\cdot\mathrm{mm}$, $5.3\,\mathrm{N}\cdot\mathrm{mm}$ and $6.4\,\mathrm{N}\cdot\mathrm{mm}$ respectively. The robot-operated catheter exhibits a similar torque pattern in the three scenarios with different thickness of soft layers, achieving maximum torques of $5.8\,\mathrm{N}\cdot\mathrm{mm}$, $6.65\,\mathrm{N}\cdot\mathrm{mm}$ and $7.77\,\mathrm{N}\cdot\mathrm{mm}$ for soft layer thicknesses of 1.0 mm, 1.5 mm, and 2.0 mm over the 5 turns rotation. The experimental results demonstrate that for all three thicknesses of soft layers, the driving force and holding torque of generated by robotic operation can satisfy the requirements of expert manual procedure. The Swan-Ganz catheter has a very flexible pre-curved tip and balloon, which have been demonstrated to be non-invasive to the patient's arteries through numerous clinical procedures. Therefore, the assessment of proximal contact force exerted by the robotically assisted catheter is not required for this study.

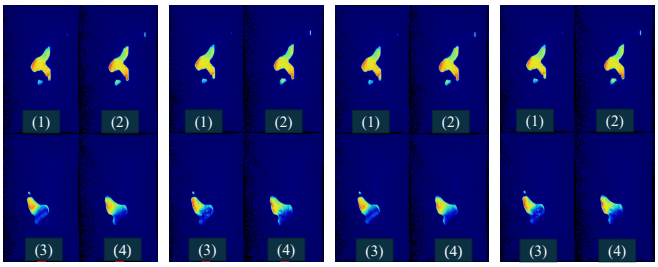

(a) PA phantom (b) Robot unpowered (c) Robot powered (d) Robot operation

Fig. 8. Experiment 2 results: (a) - (d) Selected MR images for the phantoms in (a) Scenario A, (b) Scenario B, (c) Scenario C, (d) Scenario D.

B. Experiment 2- MR conditionality evaluation

1) Experimental protocol: One significant parameter used to estimate MRI quality is the Signal-to-Noise Ratio (SNR). In Experiment 2, a water-filled phantom and the robot were placed in the bore of the MRI scanner (1.5T, Siemens MAGNETOM Aera, Siemens Healthineers, Germany). The setup for this experiment is shown in Fig. 7(a). The SNR loss was measured in the following four scenarios:

A) The PAC phantom is placed in the bore of MRI scanner.
B) The catheterization robot and phantom are positioned inside the bore of MRI scanner.
C) The robotic system is powered and located inside the MRI scanner, together with the phantom. The two motors of the robot are stationary.
D) A catheter is mounted on the robotic system navigated within the phantom.

The National Electrical Manufacturers Association (NEMA) provides an effective methodology for calculating the SNR of MR images is the two-region method [35]: One region is the signal intensity from an MR image targeting the Region-of-Interest (ROI) ($S_{mean}(ROI_{signal})$) and the other region is the signal noise for the image background outside the phantom ($SD(ROI_{back})$). Dividing $S_{mean}(ROI_{signal})$ and $SD(ROI_{back})$ will calculate the SNR for a given scenario. To assess the MR conditionality of the robot, a set of MR images were acquired for each of the four scenarios mentioned above. The SNR for scenarios B, C, and D were compared to scenario A, and the SNR of MRI images with the two-region method for each scenario was calculated based on (1). The standard deviation of the image background noise signal was then determined using (3).

TABLE II
MEASUREMENT OF SNR IN FOUR SCENARIOS.

Scenarios	Phantom	Unpowered	Powered	Operation	**SNR variation**
SNR Img_(1)	23.1799	22.7699	22.7002	22.6256	2.3913%
SNR Img_(2)	24.8200	24.1205	23.9874	23.9615	3.4589%
SNR Img_(3)	16.0311	15.7855	15.7298	15.6093	2.6362%
SNR Img_(4)	17.6241	17.3594	17.2750	17.2676	2.0536%

$$SNR(ROI) = \frac{S_{mean}(ROI_{signal})}{SD(ROI_{back})} \tag{1}$$

The average signal intensity $S_{mean}(ROI_{signal})$ in the region of interest (ROI) can be calculated as:

$$S_{mean}(ROI_{signal}) = \frac{\sum_{i=1}^{n}\sum_{j=1}^{m} V(i,j)}{mn} \tag{2}$$

Where the $V(i,j)$ is the pixel value of the image, i is the index across the read encoding direction, j is the index across the phase encoding direction, and m and n are the number of pixels in the column and row directions. The standard deviation $SD(ROI_{back})$ of the image background noise signal was then determined:

$$SD(ROI_{back}) = \left[\frac{\sum_{i=1}^{n}\sum_{j=1}^{m_i}(V(i,j)-\overline{V})^2}{\sum_{i=1}^{n}(m_i)-1}\right]^{\frac{1}{2}} \tag{3}$$

$$\overline{V} = \frac{\sum_{i=1}^{n}\sum_{j=1}^{m_i} V(i,j)}{\sum_{i=1}^{n} m_i} \tag{4}$$

Where $S_{mean}(ROI_{signal})$ is the average signal in the ROI of the phantom, $SD(ROI_{back})$ is the standard deviation of the background image noise. $\overline{V}$ is the average noise value of an ROI, 20 sets of 645 $\times$ 510 MRI images were collected for each of scenarios (A-D).

2) Results for Experiment 2:Fig. 8(a)-(d) show a color maps of selected 4 sets of MR images for the phantom under the experimental scenarios of A-D. Using the MRIqual toolbox, Region-of-Interest (ROI_{signal} and ROI_{back}) were defined to calculate the SNR using the two-region method described in Equations (1)–(4). Table II presents the measured SNR values for each scenario. Compared to Scenario A (phantom only), Scenarios B, C, and D exhibited a slight decrease in SNR. The maximum SNR variation occurred in SNR Image_(2) at 3.4589%, while the lowest variation was observed in SNR Image_(4) at 2.0536%. Across all scenarios, the average SNR variation remained below 3.5%, indicating acceptable impact on MR images during robotic operation. Furthermore, no image artifacts were observed during robot-operated patient-specific RHC interventions.

C. Experiment 3- MRI-guided robotic teleoperation

1) Experimental protocol: In this experiment, the teleoperation performance of the robot within an MRI environment was assessed, as shown in Fig. 7. Similar to Experiment 2, the setup included the interventional robot and patient-specific, water-filled cardiac phantoms, positioned within the bore. The console was positioned in the main control room, connected to the MRI room via two 10-meter-long MR-conditional cables. A 500 mm long soft silicone tube connected the robot to the cardiac phantom inlet, simulating a femoral vein vessel, with a clinically utilized catheter sheath assembled in its end. After the catheter was inserted through the sheath, the balloon at its tip was inflated. The system was then scanned at 1.5 Tesla, enabling the operator to switch views and visually track the catheter balloon on the MRI monitor in the control room (see

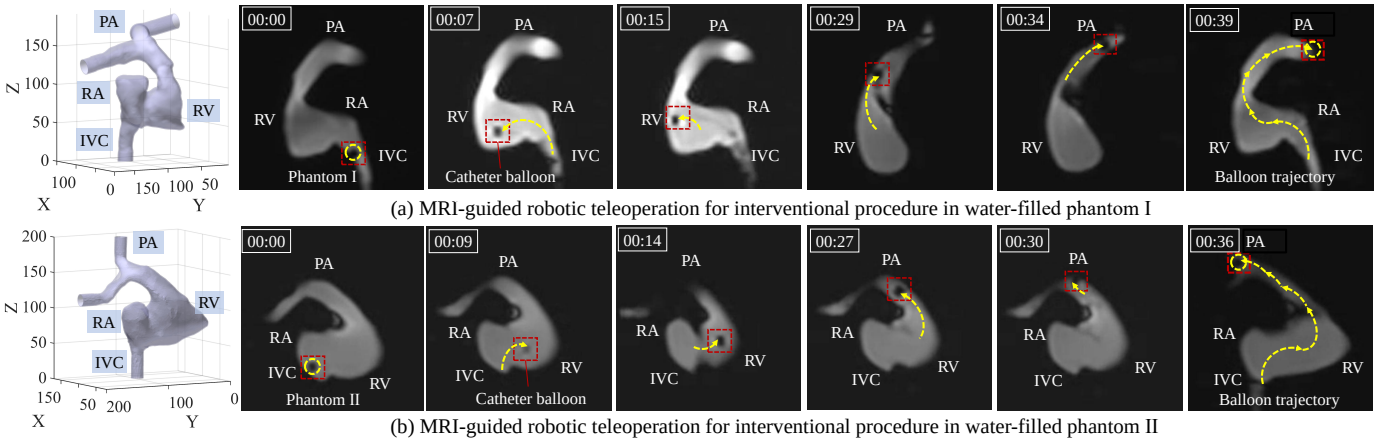

(a) MRI-guided robotic teleoperation for interventional procedure in water-filled phantom I

(b) MRI-guided robotic teleoperation for interventional procedure in water-filled phantom II

Fig. 9. Experiment 3 results: MRI-guided robotic teleoperation in water-filled patient-specific phantoms. (a) MRI-guided robotic teleoperation in phantom I. (b) MRI-guided teleoperation in phantom II.

Fig. 6 top right). This real-time visual feedback allowed the operator to remotely control the robot, adjusting the catheter's translational and rotational movements via joystick console (see Fig. 7 bottom right). For these procedures, 2 patient-specific cardiac phantoms (I and II) were utilized.

2) Results for Experiment 3: Fig. 9(a) and (b) illustrates the MRI-guided robotic teleoperation of RHC in a water-filled, patient-specific phantoms. The shaded points in the figures are catheter balloon captured in the MRI monitor, which required real-time adjustments of MRI view slices to accurately track the balloon under the MRI environment. The results demonstrate that the robotic system successfully navigated the catheter balloon from the IVC to the RA, maintaining smooth and continuous rotational and translational motion through the RV and ultimately reaching the target position in the pulmonary artery. The intervention times varied across the patient-specific phantoms, for Phantom I, which featured a stenotic pulmonary artery, the catheter balloon was successfully navigated to the PA with real-time MRI view adjustments, requiring 39s. For Phantom II, the navigation time was reduced to 36s.

D. Experiment 4- Comparison of manual and robotic operation

1) Experimental protocol: This experiment involved a comparative analysis between expert manual operation (See Section II-A) and robotic operation. Fig. 10 presents the setup, which includes the interventional robot, water-filled patient-specific phantom, camera, robot console (a), and real-time balloon position feedback interface (b). The robot console provides catheter control via four joysticks: Joystick A governs translational motion (advancement and pull back), Joystick B controls catheter rotation, Joystick C allows simultaneous translational and rotational movements, and Joystick D manages catheter balloon inflation and deflation. This configuration enables the operator to remotely manipulate the catheter through the joysticks, completing the intervention within the phantoms using the real-time balloon tracking interface. Each scenario consisted of 10 interventions per phantom, during which the time taken and the real-time 3D position of the catheter balloon were recorded. 7 patient-specific phantoms were fabricated from VeroClear material using a PolyJet Objet 500 Connex printer (Stratasys Ltd., USA).

Providing real-time visual feedback of the catheter balloon during manual and robotic teleoperation is essential. To address this challenge, a deep learning (DL)-based convolutional neural network (CNN) strategy employing the Residual Networks (ResNet) architecture is proposed. As shown in Fig. 8(11), the CNN processes pre-recorded 2D image dataset of catheter interventions aligned with 3D balloon position dataset captured by the NDI Aurora mini tracker. Image augmentation techniques including the addition of random noise, and variations in brightness, contrast, and saturation

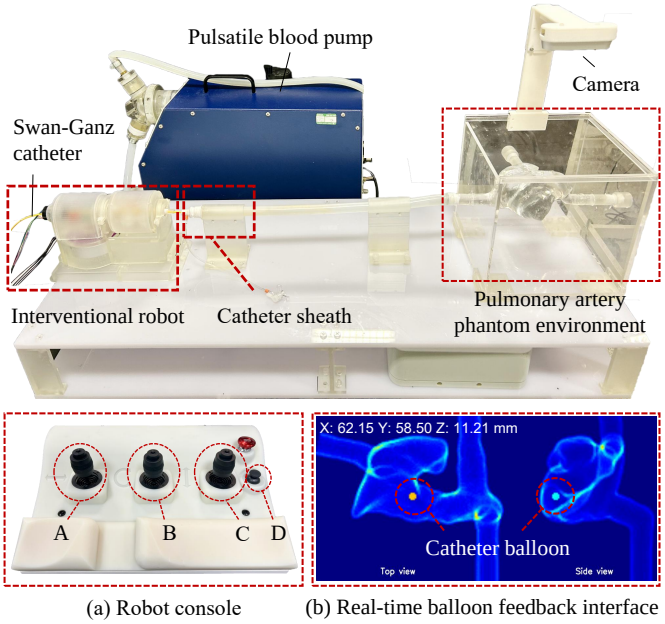

(a) Robot console (b) Real-time balloon feedback interface

Fig. 10. Experiment 4 setup: Robotic teleoperation setup, consisting of robot, camera, patient-specific phantom, and joystick console (a). The robot is controlled via joysticks to manipulate the catheter for intervention procedure under real-time balloon position feedback interface (b).

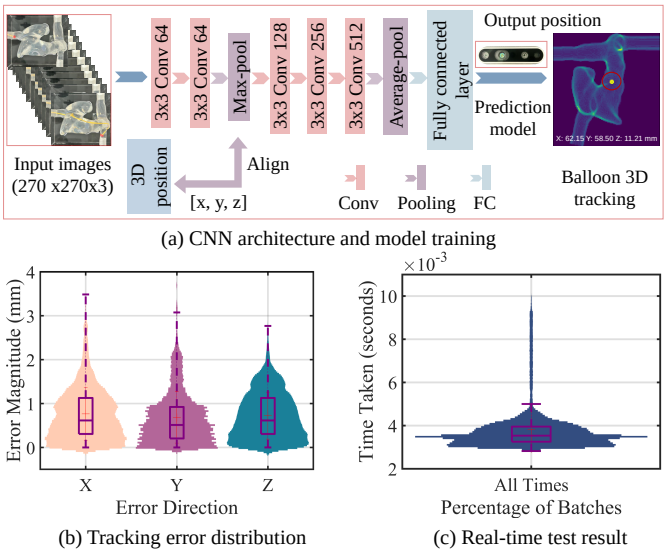

(a) CNN architecture and model training

(b) Tracking error distribution

(c) Real-time test result

Fig. 11. DL-based balloon visual feedback. (a) Input images, CNN architecture and output interface for the catheter balloon tracking. (b) A plot displaying the trained results alongside the distribution of ground-truth errors. (c) Real-time performance of the prediction model for balloon tracking.

were employed to improve robustness.

The CNN architecture is illustrated in Fig. 11(a). The network was trained 800 epochs, though over-fitting occurred beyond 700 epochs and the optimal performance was identified at 670 epochs. Training and image segmentation were conducted on an NVIDIA GeForce RTX 3080 Laptop GPU and a 12th Gen Intel® Core™ i9-12900H CPU, within a software environment comprising PyTorch 1.8, CUDA Toolkit 11.1, cuDNN 8.1.1, and Python 3.9. Using the NDI Aurora tracker's data as ground truth, the prediction model demonstrated a localization accuracy within a 3mm error margin (Fig. 11(b)), with a mean prediction time of only 0.0036s per frame (Fig. 11(c)).

2) Results for Experiment 4: Fig. 12(a) illustrates robot-operated interventions for 7 patient-specific phantoms, and the results show that the robot can successfully manipulate the catheter to complete the task for phantoms with different geometries, i.e., the catheter's balloon travels from the IVC to the target position of PA.

Fig. 12(b) shows the trajectories of the catheter balloon for each phantom operated by the robot for 10 operations. To assess the consistency of catheter trajectories, the Root Mean Square Error (RMSE) is employed as a quantitative metric. Since both manual and autonomous RHC procedures follow a consistent anatomical path—IVC → RA → RV → PA—all trajectories are uniformly resampled to enable direct comparison. Each trajectory is resampled to $K = 200$ discrete points, denoted by the index k, where $k \in \{1, \ldots, K\}$.

For each trajectory type, manual (m) and robotic (r), the mean trajectory is computed by averaging the spatial positions across all trials at each resampled index k:

$$\bar{T}_s(k) = \frac{1}{N_s} \sum_{i=1}^{N_s} (x^i_{s,k}, y^i_{s,k}, z^i_{s,k}), \quad s \in \{m, r\} \tag{5}$$

where N_s represents the number of trajectories in scenario s, and $(x^i_{s,k}, y^i_{s,k}, z^i_{s,k})$ denotes the 3D position of the catheter at point k for trajectory i. In this study, $N_m = N_r = 10$.

The RMSE is computed separately for manual and robotic trajectories to quantify the deviation of each trajectory from its corresponding mean trajectory:

$$RMSE_s = \sqrt{\frac{1}{N_s K} \sum_{i=1}^{N_s} \sum_{k=1}^{K} d(p^i_{s,k}, \bar{T}_s(k))^2}, \quad s \in \{m, r\} \tag{6}$$

Where $p^i_{s,k} = (x^i_{s,k}, y^i_{s,k}, z^i_{s,k})$ represents the 3D coordinates of the trajectory at index k, and the Euclidean distance to the mean trajectory is given by:

$$d(p^i_{s,k}, \bar{T}_s(k)) = \sqrt{(x^i_{s,k} - \bar{x}_{s,k})^2 + (y^i_{s,k} - \bar{y}_{s,k})^2 + (z^i_{s,k} - \bar{z}_{s,k})^2} \tag{7}$$

Where $\bar{x}_{s,k}, \bar{y}_{s,k}, \bar{z}_{s,k}$ are the mean spatial positions of all trajectories at each resampled point k.

Table III presents the RMSE of catheter trajectories for both manual and robotic operations across different patient-specific cases (A–G). The results demonstrate that robotic operation consistently achieves lower RMSE values compared to manual operation across all patient cases, indicating improved trajectory consistency with robotic assistance. Specifically, the mean RMSE for manual operation across all cases is 7.85mm, whereas robotic operation achieves a mean RMSE of 5.19mm, corresponding to a 33.9% reduction in trajectory deviation. The most notable improvement is observed in Phantom C, where RMSE is reduced from 9.86mm to 6.97mm, demonstrating the system's ability to enhance catheter navigation consistency even in complex anatomical regions.

Fig. 13(a) records the time required for manual and robotic operation by expert. The duration of expert manual procedures varied significantly, with the most time-consuming for Phantom C reaching 59.64 s, and for Phantoms E and G, exceeding 40 s. In contrast, all robotic procedures were completed within 40 s, with the longest duration being 30.66 s for Phantom C. Fig. 13(b) provides an overall comparison, indicating that the average duration for manual and robotic procedures was 7.74 s and 11.58 s, respectively. Notably, the robotic system demonstrated efficiency, completing PA interventions within a reduced time range of 3.66 s to 20.40 s compared the manual operation (3.05 s to 25.64 s) across the 7 patient-specific phantoms.

IV. Discussion of Results

In Experiment 1, during the evaluation of driving force and torque, the active-passive rollers generate higher friction and

TABLE III
RMSE OF TRAJECTORIES FOR MANUAL VS. ROBOTIC OPERATION (MM).

Patient-specific	A	B	C	D	E	F	G
Manual operation	7.545	6.541	9.860	7.259	7.656	9.079	7.965
Robot operation	4.873	4.750	6.972	4.490	5.040	6.977	5.151

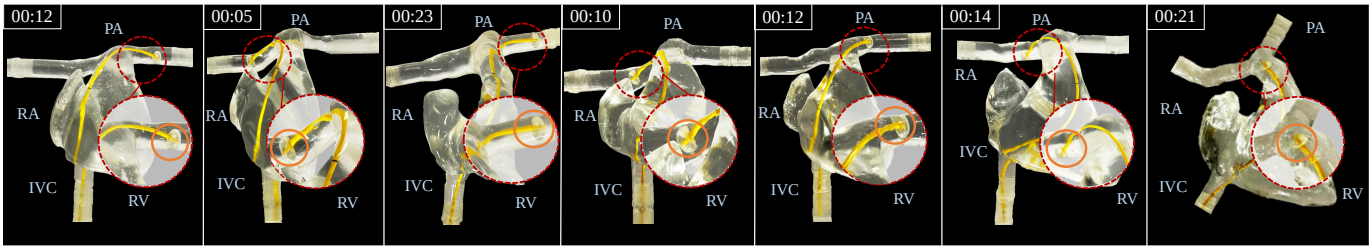

(a) Robotic teleoperated Swan-Ganz catheter for water-filled patient-specific phantom interventions from IVC to PA

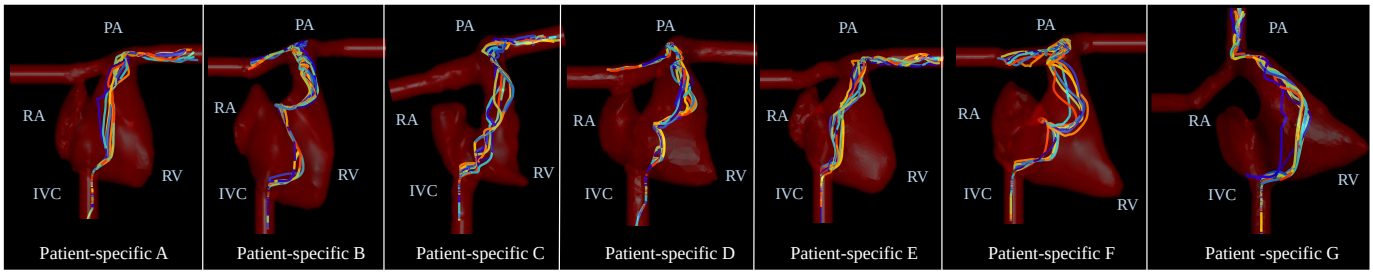

(b) Trajectories of catheter balloon in repeated interventions of robotic teleoperation within 7 patient-specific phantoms

Fig. 12. Experiment 3 results. (a) Robotic teleoperated interventions within 7 water-filled patient-specific phantoms. (b) Trajectories of catheter balloon for repeated robotic interventions.

torque on the catheter when a soft material with more thickness of the soft layer is applied. This can be attributed to the fact that more thickness of soft material provides a larger contact area for the catheter, resulting in a greater clamping force. Additionally, for torque evaluation, increasing the degree of rotation of the catheter while it is fixed to the force-torque sensor will enhance the torque of the robotic operation on the catheter eventually reach a constant value. By varying the thickness of the soft layer, the robot demonstrated the ability to achieve different levels of friction and torque. This versatility significantly enhances its applicability to various levels of complexity encountered phantom scenarios.

Experiment 2 evaluated the MR conditionality of the robotic system during right heart catheterization procedures under MRI guidance. A marginal reduction in SNR was observed relative to the baseline (Scenario A), with the most pronounced decrease occurring during robot operation. This reduction is attributed to the electromagnetic interference generated by the ultrasonic piezoelectric motors (USMs) and the current. Notably, the lowest SNR values coincided with the robot's working state—when simultaneous translational and rotational

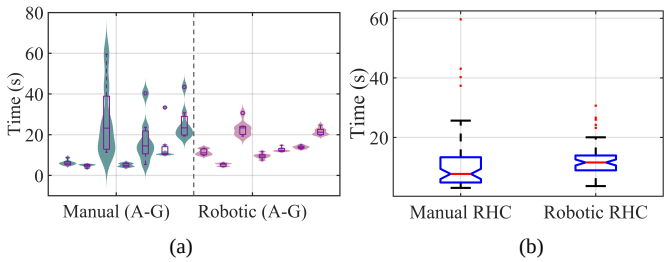

Fig. 13. Experiment 3 results: (a) Distribution of time required for manual and robotic manipulation within 7 patient-specific phantoms (b) Overall comparison between manual and robotic operation from the clinical expert.

catheter movements were executed—suggesting that actuation-related current fluctuations introduced disturbances to the MR imaging. Nevertheless, the overall SNR variation remained below 3.5%, which is well within the acceptable variation for MR-conditional devices. No image artifacts or signal distortions were observed in any of the MRI slices across all test scenarios. These results validate the MR conditionality of the proposed robotic system and demonstrate its feasibility for safe integration into MRI-guided clinical workflows.

In Experiment 3, compared to robotic teleoperation of RHC outside the MRI environment with real-time visual feedback, MRI-guided robotic teleoperation required extended operation time. This time-consumption was primarily due to the need for continuous viewpoint adjustments during real-time MRI tracking of the catheter balloon. Such adjustments are essential to maintain accurate visualization and ensure reliable navigation feedback to the operator. This operation reflects one of the inherent limitations of MRI for interventional procedures, where imaging latency and the absence of continuous visualization introduce operational delays. In addition to imaging constraints, broader challenges limit the adoption of MRI in cardiovascular interventions, including the limited availability of MR-conditional instruments, the need for specialized MR-conditional robotic components that can operate safely and effectively within high magnetic field environments, as well as the substantial cost and infrastructure demands associated with MRI-based interventional settings. Despite these challenges and limitations, the MR-conditional robotic system proposed in this study shows strong potential to improve healthcare workflow efficiency, MRI-guided robot-assisted RHC will provide radiation-free, highly consistent catheter navigation during interventional procedures on patients.

In Experiment 4, the performance of robotic operation across 7 patient-specific intra-phantom interventions returned

time consistency compared to manual operation. This enhanced performance is attributed to the robot's ability to execute (simultaneous) infinite continuous translational and rotational movements. The coupled translational and rotational motion will robustly navigate the catheter from the RA to the RV during RHC surgery, which is challenging to achieve with manual RHC. Table III summarizes the comparison of the RMSE of manual and robotic RHC balloon trajectories, showing that robotic interventions of patient-specific phantoms have improved trajectory consistency performance.

V. Conclusions

This paper presents an MR-conditional robotic system that enables (simultaneous) infinite continuous translational and rotational movement of the inserted catheter during right heart catheterization. The system successfully enabled MRI-guided, robot-assisted patient-specific interventions in phantoms, providing enhanced maneuverability. Ultrasound piezoelectric motors were employed for actuation, allowing the robot can be flexibly positioned both at outside and inside of MRI scanner bore and access to the entry point (jugular vein or femoral vein). Comparing our robotic platform with the literature highlights the contribution of our proposed system. Experiments validated the low interference of our robot with MRI and demonstrate the system's capability to achieve a range of force and torque values at the clinical catheter. Robotic teleoperation demonstrated enhanced consistency compared to manual operation by an expert clinician. Moreover, MRI-guided robotic teleoperation enabled successful interventions in patient-specific phantoms.

Future work will concentrate on the deployment of robot sterilization and as well as on preclinical validation of MRI-guided robotic operation in animal cardiovascular interventions. Furthermore, to enhance the autonomy of robot-assisted catheterization procedures, Reinforcement Learning (RL) algorithms will be integrated, paving the way for autonomous robot-assisted right heart interventions.

References

[1] M. Vaduganathan, G. A. Mensah, J. V. Turco, V. Fuster, and G. A. Roth, "The global burden of cardiovascular diseases and risk," *Journal of the American College of Cardiology*, vol. 80, no. 25, pp. 2361–2371, 2022.

[2] Y. R. Manda and K. M. Baradhi, *Cardiac Catheterization Risks and Complications*. StatPearls Publishing, Treasure Island (FL), 2022. [Online]. Available: http://europepmc.org/books/NBK531461

[3] X. Jin, S. Guo, J. Guo, P. Shi, T. Tamiya, M. Kawanishi, and H. Hirata, "Total force analysis and safety enhancing for operating both guidewire and catheter in endovascular surgery," *IEEE Sensors Journal*, vol. 21, no. 20, pp. 22 499–22 509, 2021.

[4] M. K. Badawy, P. Deb, R. Chan, and O. Farouque, "A review of radiation protection solutions for the staff in the cardiac catheterisation laboratory," *Heart, Lung and Circulation*, vol. 25, no. 10, pp. 961–967, 2016.

[5] X. Yin, S. Guo, N. Xiao, T. Tamiya, H. Hirata, and H. Ishihara, "Safety operation consciousness realization of a mr fluids-based novel haptic interface for teleoperated catheter minimally invasive neurosurgery," *IEEE/ASME Transactions on Mechatronics*, vol. 21, no. 2, pp. 1043–1054, 2016.

[6] H. Su, K.-W. Kwok, K. Cleary, I. Iordachita, M. C. Cavusoglu, J. P. Desai, and G. S. Fischer, "State of the art and future opportunities in mri-guided robot-assisted surgery and interventions," *Proceedings of the IEEE*, vol. 110, no. 7, pp. 968–992, 2022.

[7] M. U. Farooq and S. Y. Ko, "A decade of mri compatible robots: Systematic review," *IEEE Transactions on Robotics*, vol. 39, no. 2, pp. 862–884, 2023.

[8] G. Li, H. Su, G. A. Cole, W. Shang, K. Harrington, A. Camilo, J. G. Pilitsis, and G. S. Fischer, "Robotic system for mri-guided stereotactic neurosurgery," *IEEE Transactions on Biomedical Engineering*, vol. 62, no. 4, pp. 1077–1088, 2015.

[9] N. A. Patel, C. J. Nycz, P. A. Carvalho, K. Y. Gandomi, R. Gondokaryono, G. Li, T. Heffter, E. C. Burdette, J. G. Pilitsis, and G. S. Fischer, "An integrated robotic system for mri-guided neuroablation: Preclinical evaluation," *IEEE Transactions on Biomedical Engineering*, vol. 67, no. 10, pp. 2990–2999, 2020.

[10] Z. He, J. Dai, J. Ho, H. Tong, X. Wang, G. Fang, L. Liang, C. Cheung, Z. Guo, H. Chang, I. Iordachita, R. Taylor, W. Poon, D. Chan, and K. Kwok, "Interactive multi-stage robotic positioner for intra-operative mri-guided stereotactic neurosurgery," *Advanced Science*, vol. 11, no. 7, Feb. 2024, publisher Copyright: © 2023 The Authors. Advanced Science published by Wiley-VCH GmbH.

[11] H. Su, W. Shang, G. Cole, G. Li, K. Harrington, A. Camilo, J. Tokuda, C. M. Tempany, N. Hata, and G. S. Fischer, "Piezoelectrically actuated robotic system for mri-guided prostate percutaneous therapy," *IEEE/ASME Transactions on Mechatronics*, vol. 20, no. 4, pp. 1920–1932, 2015.

[12] H. Liang, W. Zuo, D. Kessler, T. Barrett, and Z. T. H. Tse, "A pneumatic driven mri-guided robot system for prostate interventions," *IEEE Transactions on Medical Robotics and Bionics*, vol. 6, no. 3, pp. 951–960, 2024.

[13] B. Yang, S. Roys, U.-X. Tan, M. Philip, H. Richard, R. P. Gullapalli, and J. P. Desai, "Design, development, and evaluation of a master–slave surgical system for breast biopsy under continuous mri," *The International Journal of Robotics Research*, vol. 33, no. 4, pp. 616–630, 2014.

[14] Y. Kim, S. S. Cheng, M. Diakite, R. P. Gullapalli, J. M. Simard, and J. P. Desai, "Toward the development of a flexible mesoscale mri-compatible neurosurgical continuum robot," *IEEE Transactions on Robotics*, vol. 33, no. 6, pp. 1386–1397, 2017.

[15] V. Groenhuis, F. J. Siepel, J. Veltman, and S. Stramigioli, "Design and characterization of stormram 4: An mri-compatible robotic system for breast biopsy," in *2017 IEEE/RSJ International Conference on Intelligent Robots and Systems (IROS)*, 2017, pp. 928–933.

[16] G. Li, N. A. Patel, Y. Wang, C. Dumoulin, W. Loew, O. Loparo, K. Schneider, K. Sharma, K. Cleary, J. Fritz, and I. Iordachita, "Fully actuated body-mounted robotic system for mri-guided lower back pain injections: Initial phantom and cadaver studies," *IEEE Robotics and Automation Letters*, vol. 5, no. 4, pp. 5245–5251, 2020.

[17] T. Liu, N. Lombard Poirot, T. Greigarn, and M. Cenk Çavuşoğlu, "Design of a Magnetic Resonance Imaging Guided Magnetically Actuated Steerable Catheter," *Journal of Medical Devices*, vol. 11, no. 2, p. 021004, 05 2017. [Online]. Available: https://doi.org/10.1115/1.4036095

[18] K.-H. Lee, K. C. D. Fu, Z. Guo, Z. Dong, M. C. W. Leong, C.-L. Cheung, A. P.-W. Lee, W. Luk, and K.-W. Kwok, "Mr safe robotic manipulator for mri-guided intracardiac catheterization," *IEEE/ASME Transactions on Mechatronics*, vol. 23, no. 2, pp. 586–595, 2018.

[19] M. Tavallaei, M. Lavdas, D. Gelman, and M. Drangova, "Magnetic resonance imaging compatible remote catheter navigation system with 3 degrees of freedom," *International Journal of Computer Assisted Radiology and Surgery*, vol. 11, pp. 1537–1545, 2016.

[20] D. Kundrat, G. Dagnino, T. M. Y. Kwok, M. E. M. K. Abdelaziz, W. Chi, A. Nguyen, C. Riga, and G.-Z. Yang, "An mr-safe endovascular robotic platform: Design, control, and ex-vivo evaluation," *IEEE Transactions on Biomedical Engineering*, vol. 68, no. 10, pp. 3110–3121, 2021.

[21] G. Dagnino, D. Kundrat, T. M. Y. Kwok, M. E. M. K. Abdelaziz, W. Chi, A. Nguyen, C. Riga, and G.-Z. Yang, "In-vivo validation of a novel robotic platform for endovascular intervention," *IEEE Transactions on Biomedical Engineering*, vol. 70, no. 6, pp. 1786–1794, 2023.

[22] Z. Dong, X. Wang, G. Fang, Z. He, J. D.-L. Ho, C.-L. Cheung, W. L. Tang, X. Xie, L. Liang, H.-C. Chang, C. K. Ching, and K.-W. Kwok, "Shape tracking and feedback control of cardiac catheter using mri-guided robotic platform—validation with pulmonary vein isolation simulator in mri," *IEEE Transactions on Robotics*, vol. 38, no. 5, pp. 2781–2798, 2022.

[23] Z. Dong, Z. Guo, K.-H. Lee, G. Fang, W. L. Tang, H.-C. Chang, D. T. M. Chan, and K.-W. Kwok, "High-performance continuous hydraulic motor for mr safe robotic teleoperation," *IEEE Robotics and Automation Letters*, vol. 4, no. 2, pp. 1964–1971, 2019.

[24] M. E. M. K. Abdelaziz, D. Kundrat, M. Pupillo, G. Dagnino, T. M. Y. Kwok, W. Chi, V. Groenhuis, F. J. Siepel, C. Riga, S. Stramigioli, and

G.-Z. Yang, "Toward a versatile robotic platform for fluoroscopy and mri-guided endovascular interventions: A pre-clinical study," in *2019 IEEE/RSJ International Conference on Intelligent Robots and Systems (IROS)*, 2019, pp. 5411–5418.

[25] Y. Chen, I. S. Godage, Z. T. H. Tse, R. J. Webster, and E. J. Barth, "Characterization and control of a pneumatic motor for mr-conditional robotic applications," *IEEE/ASME Transactions on Mechatronics*, vol. 22, no. 6, pp. 2780–2789, 2017.

[26] J. Sheng, X. Wang, T.-M. L. Dickfeld, and J. P. Desai, "Towards the development of a steerable and mri-compatible cardiac catheter for atrial fibrillation treatment," *IEEE Robotics and Automation Letters*, vol. 3, no. 4, pp. 4038–4045, 2018.

[27] K. G. Chan, T. Fielding, and M. Anvari, "An image-guided automated robot for mri breast biopsy," *The International Journal of Medical Robotics + Computer Assisted Surgery: MRCAS*, vol. 12, no. 3, pp. 461–477, 2016.

[28] Y. Kim, S. S. Cheng, M. Diakite, R. P. Gullapalli, J. M. Simard, and J. P. Desai, "Toward the development of a flexible mesoscale mri-compatible neurosurgical continuum robot," *IEEE Transactions on Robotics*, vol. 33, no. 6, pp. 1386–1397, 2017.

[29] D. B. Comber, J. E. Slightam, V. R. Gervasi, J. S. Neimat, and E. J. Barth, "Design, additive manufacture, and control of a pneumatic mr-compatible needle driver," *IEEE Transactions on Robotics*, vol. 32, no. 1, pp. 138–149, 2016.

[30] M. A. Tavallaei, Y. Thakur, S. Haider, and M. Drangova, "A magnetic-resonance-imaging-compatible remote catheter navigation system," *IEEE Transactions on Biomedical Engineering*, vol. 60, no. 4, pp. 899–905, 2013.

[31] S. Aggarwal, E. Choudhury, S. Ladha, P. Kapoor, and U. Kiran, "Simulation in cardiac catheterization laboratory: Need of the hour to improve the clinical skills," *Annals of Cardiac Anaesthesia*, vol. 19, p. 521, 2016.

[32] G. Li, H. Su, G. A. Cole, W. Shang, K. Harrington, A. Camilo, J. G. Pilitsis, and G. S. Fischer, "Robotic system for mri-guided stereotactic neurosurgery," *IEEE Transactions on Biomedical Engineering*, vol. 62, no. 4, pp. 1077–1088, 2015.

[33] G. Li, N. A. Patel, E. C. Burdette, J. G. Pilitsis, H. Su, and G. S. Fischer, "A fully actuated robotic assistant for mri-guided precision conformal ablation of brain tumors," *IEEE/ASME Transactions on Mechatronics*, vol. 26, no. 1, pp. 255–266, 2021.

[34] M. Wartenberg, J. Schornak, K. Gandomi, P. Carvalho, C. Nycz, N. Patel, I. Iordachita, C. Tempany, N. Hata, J. Tokuda, and G. Fischer, "Closed-loop active compensation for needle deflection and target shift during cooperatively controlled robotic needle insertion," *Annals of Biomedical Engineering*, vol. 46, 2018.

[35] Z. Hornberger, "Determination of signal-to-noise ratio (snr) in diagnostic magnetic resonance imaging," *National Electrical Manufacturers Association*, pp. 1–19, 2021.

VI. Biography Section

Yaxi Wang (Student Member, IEEE) received an MSc degree in Electromechanical Engineering with the interneational study from the University of Macau, China, 2020. He is currently pursuing a Ph.D degree in medical robotics from University College London, UK. His research intersets include MR-conditional robotics and Machine learning for autonomy of medical/interventional robotics.

Enhui Yong received the M.B. and B.S. degree in Medicine from Barts and the London, Queen Mary University of London, in 2012. He is currently pursuing a Ph.D in Cardiovascular Biomedicine at the Institute of Cardiovascular Science, University College London. His research interests are on computational modelling of coronary flow.

Wenlong Gaozhang (Student Member, IEEE) received the B.S. degree in Mechanical Engineering from the Xiamen University, China, in 2017, and the M.S. degree Mechanical Engineering from the Xi'an Jiaotong University, China, in 2020. He is currently pursuing the Ph.D degree in Mechanical Engineering at University College London, London, UK. His research interests include soft robotics and collaborative robots.

Vivek Muthurangu is Professor of Cardiovascular Imaging and Physics at University College London, Head of Research Department of Children's Cardiovascular Disease, Chair of iBSc board of examiners. He received a degree (B.M. and B.S.) from University of Edinburgh, and a PhD in Medicine from King's College London in 2007. Vivek has authored over 200 articles, published in high-impact journals, peer-reviewed full-length conference papers.

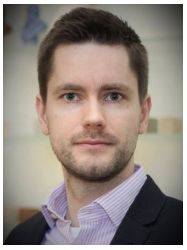

Helge A Wurdemann (Member, IEEE) is Professor of Robotics at University College London leading the Soft Haptics and Robotics lab. He received a degree (Dipl. Ing.) in electrical engineering with a focus on mechatronics and robotics in the medical field from the Leibniz University of Hanover, and a PhD in Robotics from King's College London in 2012. Helge has authored over 100 articles, published in high-impact journals, peer-reviewed full-length conference papers, and presented at leading robotics conferences.